The Astrophysical Journal, 922:64 (9pp), 2021 November 20 https://doi.org/10.3847/1538-4357/ac23cc

The Structural Connection between Coronal Mass Ejection Flux Ropes near the Sun and at 1 au

H. Xie[1,2], N. Gopalswamy[2], and S. Akiyama[1,2]
[1] Department of Physics, The Catholic University of America, Washington DC, USA; hong.xie@nasa.gov
[2] Solar Physics Laboratory, NASA Goddard Space Flight Center, Greenbelt, MD, USA
Received 2021 July 30; revised 2021 September 2; accepted 2021 September 2; published 2021 November 19

Abstract

We have performed the first comprehensive statistical analysis comparing flux rope (FR) structures of coronal mass ejections (CMEs) near the Sun and at 1 au, using Solar and Heliospheric Observatory and Solar Terrestrial Relations Observatory measurements for the two full solar cycles 23 and 24. This study aims to investigate the physical connection of 102 magnetic FRs among solar source regions, CMEs in the extended corona, and magnetic clouds (MCs) near Earth. Our main results are as follows: (1) We confirmed that the hemispheric-helicity rule holds true for ∼87% of our 102 events. For the 13 events that do not follow this rule, the FR axis directions and helicity signs can be inferred from soft X-ray and extreme ultraviolet images and magnetogram data in the source regions (e.g., coronal arcade skews, Fe XII stalks, sigmoids, and magnetic tongues). (2) Around 25% of the 102 events have rotations >40° between the MC and CME-FR axial orientations. (3) For ∼56% of these rotational events, the FR rotations occurred within the COR2 field of view, which can be predicted from the CME tilts obtained from FR fitting models. In addition, we found that for 89% of the 19 stealth CMEs under study, we were able to use coronal neutral line locations and tilts to predict the FR helicity and its axial direction in the MCs. The above results should help improve the prediction of FR structures in situ. We discuss their implications on space weather forecasts.

Unified Astronomy Thesaurus concepts: Solar coronal mass ejections (310); Solar magnetic fields (1503); Solar filament eruptions (1981); Solar flares (1496); Interplanetary magnetic fields (824)

1. Introduction

A magnetic flux rope (MFR) structure consists of helical magnetic field lines twisting around its axial field, which is the key structure in coronal mass ejections (CMEs) and their solar source regions. In the past decades, substantial evidence based on modeling and observations has been accumulated indicating that most CMEs contain an MFR structure (e.g., Chen et al. 1997; Dere et al. 1999; Gibson & Low 2000; Krall & Cyr 2006; Chen 2011; Gopalswamy et al. 2013a; Mäkelä et al. 2013; Xie et al. 2013; Yashiro et al. 2013; Vourlidas 2014). CMEs in white-light coronagraphs from the limb typically show a three-part flux rope (FR)-like structure, i.e., a bright frontal loop followed by a dark cavity with an embedded core (Illing & Hundhausen 1985). The dark cavity is believed to be the MFR structure. In recent high-cadence extreme ultraviolet (EUV) observations by the Atmospheric Imaging Assembly (AIA; Lemen et al. 2012) on board the Solar Dynamics observatory (SDO; Pesnell et al. 2012), MFRs have been detected in both cool and hot EUV passbands (e.g., Cheng et al. 2011, 2013; Zhang et al. 2012; Nindos et al. 2020), where hot FR-like structures tend to be enclosed in a dark cavity of cool EUV passbands (e.g., Veronig et al. 2018). As one example of the direct evidence, interplanetary CMEs (ICMEs) often show MFR structures, known as magnetic clouds (MCs; e.g., Burlaga et al. 1981; Burlaga 1988). Gopalswamy (2006) suggested that all ICMEs have MFR structures, but their propagation directions determine whether they can be observed by the spacecraft in situ (e.g., Xie et al. 2013). Since MCs, specifically, the long duration southward magnetic fields in MCs (and associated shock sheaths) are the primary cause of geomagnetic storms (Wu et al. 2006; Gopalswamy et al. 2015), studying the connection between the MC and CME-FR structures is of crucial importance to space weather forecasting.

Previous studies have shown that a CME FR may change its direction and axial orientation when propagating from the Sun to Earth, i.e., the CME deflection and rotation. It is well known that CMEs near the solar minimum tend to be deflected toward the solar equator by the strong open magnetic fields of coronal holes (e.g., Gopalswamy et al. 2003, 2008, 2009; Xie et al. 2009; Kay et al. 2017). Shen et al. (2011) used the gradient of magnetic energy density to explain the deflection of CMEs in the low corona. Recent studies have shown that CMEs can be deflected not only by the large-scale structures but can also be channeled by the strong magnetic fields near active regions (ARs; e.g., Sterling et al. 2011; Gopalswamy et al. 2014; Möstl et al. 2015; Liu et al. 2018). On the other hand, whether a CME FR experiences a large amount of rotation and where most of the rotation occurs is still up for debate. Previous theoretical models and numeric simulations have shown that large rotations (>50°–120°) occurred during the CME eruption in the low corona (Fan & Gibson 2004; Török et al. 2004; Lynch et al. 2009; Kay et al. 2017). They also found a helicity-rotation pattern, i.e., positive (negative) FRs rotate clockwise (counterclockwise), due to a kink instability or magnetic tension forces. Observational analysis based on case studies or a small sample has also presented evidence for large rotations during the CME eruption and propagation from the Sun to Earth (e.g., Green et al. 2007; Vourlidas et al. 2011; Palmerio et al. 2018). In contrast, Marubashi et al. (2015) conducted a statistical study using 54 ICMEs selected for the 2011 and 2012 Coordinated Data Analysis Workshops (CDAWs; Gopalswamy et al. 2013b). They argued that the MFR orientation maintained within ±25° between MC-CME pairs if choosing the right fitting models, i.e., a cylindrical or a toroidal force-free FR

model. Yurchyshyn et al. (2007) found that for ∼64% of their well-established 25 MC-CME pairs, the MC orientation is within ±45° of the CME orientation. In addition, Yurchyshyn (2008) compared the MFR orientation with that of coronal neutral lines (CNLs) and speculated that the orientation of CNLs may have some influence on the evolution of the MFR structure.

In this paper, we use a comprehensive data set, including two full solar cycles (SCs) 23 and 24, to study the evolution of the MFR structure. This is the first comprehensive statistical study on the comparison of MC and CME-FR structures. In Xie et al. (2013), we applied an elliptical FR (EFR) model developed by Krall & Cyr (2006) to study MC-CME events. As a continuation study, we conduct the same EFR model fit to obtain the CME orientations for SC 24 events and compare them with the initial FR structures in their solar source regions and MC magnetic structures in situ. In addition, we study the relation between streamer-blowout CMEs, CNLs, and MCs near solar minima.

The paper is organized as follows. In Section 2, we describe the event selection, observational data, and methods we used to determine the MFR structures in MC-CME events. In Section 3, we present our statistical results for the 102 events, including the relation between CME source locations and MC helicity signs, the helicity-rotation pattern, and a table listing all of the large rotational events. Finally, in Section 4, we provide a discussion and summary of the study.

2. Data and Methods

Our study started with the MC list observed by the Wind spacecraft, whose fitting parameters are published in Lepping et al. (2006, 2011, 2015, 2018, 2020; the Lepping MC list hereafter). To find the CME candidate for each MC, we searched in a time window of ∼1–3 days from the rough CME time tracing back from the average MC speed. To ensure the correct MC-CME pair, we also check the CME travel time using the empirical CME arrival model by Gopalswamy et al. (2000). The CME online catalogs we used in the study include the CDAW LASCO CME list,[3] SECCHI COR1[4], and COR2 lists,[5] where the CME observations are from the Large Angle and Spectroscopic Coronagraph (LASCO; Brueckner et al. 1995) on board the Solar and Heliospheric Observatory (SOHO) Mission (Domingo et al. 1995) and the Sun–Earth Connection Coronal and Heliospheric Investigation (SECCHI; Howard et al. 2008) on board the Solar Terrestrial Relations Observatory (STEREO) mission (Kaiser et al. 2008). We selected 102 MC-CME pairs from 1996–2020 based on the following criteria: (1) MC-CME pairs have a unique and clear match and (2) B_z or B_y components in MCs show clear rotation with an axial field magnitude in B_y or $B_z \geqslant 5$ nT. We have excluded complex events involved with multiple CMEs where individual characteristics of MCs were not visible. Also, we excluded MC events whose axes are aligned largely in the Sun–Earth direction (within ±20°) and where the observing spacecraft may cross one of the FR legs. Note that the Lepping MC list only covers the period from 1996–2015. From 2016–2020, we used the OMNI data (http://omniweb.gsfc.nasa.gov) to identify the MCs based on the definition in Burlaga et al. (1981): (i) enhanced magnetic field intensity, (ii) smooth rotation of the magnetic field, and (iii) low proton temperature and low plasma beta. We identified the MC boundaries by requiring that the proton temperature (T_p) falls below the expected solar wind proton temperature (Lopez & Freeman 1986) and/or the plasma beta is <1. We also used the magnetic field rotation and discontinuities to adjust the boundaries accordingly. The MC fitting parameters were obtained by applying a simple cylindrical force-free FR model using the least-squares fitting process (e.g., Burlaga 1988; Lepping et al. 1990). The fitting parameters were determined in the geocentric solar ecliptic coordinate system, where the *y*-axis is in the ecliptic plane pointing toward the east, the *x*-axis is directed from the Earth toward the Sun, and the *z*-axis is pointed northward. We define an MC tilt angle as positive for a clockwise (CW) rotation and negative for a counterclockwise (CCW) rotation from the *y*-axis (east). The tilt angle can be derived from latitude and longitude using a coordinate transformation (e.g., Xie et al. 2004; Marubashi et al. 2015).

To determine CME-FR tilt angles, we applied the EFR model (Krall & Cyr 2006) to LASCO observations for SC 23 events and to both SECCHI and LASCO observations for SC 24 events. The tilt in the EFR model is defined as CW from east of the FR axis. Note that the CME tilt obtained from the EFR model has an 180° ambiguity in the magnetic field direction along the axis. To remove the ambiguity, we use observations from solar source regions to infer the direction of the magnetic field (e.g., Gopalswamy et al. 2018; Sarkar et al. 2020).

For CMEs associated with filament eruptions, the FR axial and poloidal field directions can be determined by the connectivity between sheared polarities along and across the photospheric polarity inversion line (PIL) in magnetograms. The magnetic chirality can be obtained by combining the axial direction and poloidal direction of the magnetic field (e.g., Marubashi et al. 2015). The FR chirality can also be deduced from the pattern of observed Hα fibrils and the skew of X-ray coronal arcades over filament channels (e.g., Martin 1998; McAllister et al. 1998; Martin et al. 2008). A very effective new method for determining the direction of the axial field in PILs is to track the evolution of the Fe XII loop legs or *stalks* rooted along the PILs using SDO/AIA 193 Å images (Sheeley et al. 2013; Wang et al. 2013). The stalks initially cross the PIL in the transverse direction, but increasingly point in the direction of the PIL as opposite-polarity flux is canceled at the PIL; the helicity sign can then easily be determined by comparing the footpoint location of the stalk with a magnetogram. It is also shown in Wang & Berger (2018) that CMEs and filament eruptions remove only a fraction of the helicity; the axial field and the remaining helicity associated with it may eventually be resubmerged via flux cancellation.

For flare CMEs associated with complex ARs, where the PIL might be curved or too compact to identify the polarity shear direction, we use solar magnetic proxies to analyze the MFR structure, including magnetic tongues, soft X-ray, and/or EUV sigmoids (Palmerio et al. 2017, and references therein). Magnetic tongues are two elongated magnetic polarities, which usually occur during the AR emerging phase as the apex of twisted flux tube emerges. The helicity sign can be estimated by analyzing its polarity pattern in magnetograms (e.g., Luoni et al. 2011). Sigmoids are S-shaped magnetic structures often observed in soft X-ray or EUV images, which are believed to be coronal tracers of an FR (e.g., Canfield et al. 1999; Titov &

[3] https://cdaw.gsfc.nasa.gov/CME_list/
[4] https://cor1.gsfc.nasa.gov/catalog/
[5] http://spaceweather.gmu.edu/seeds/secchi.php

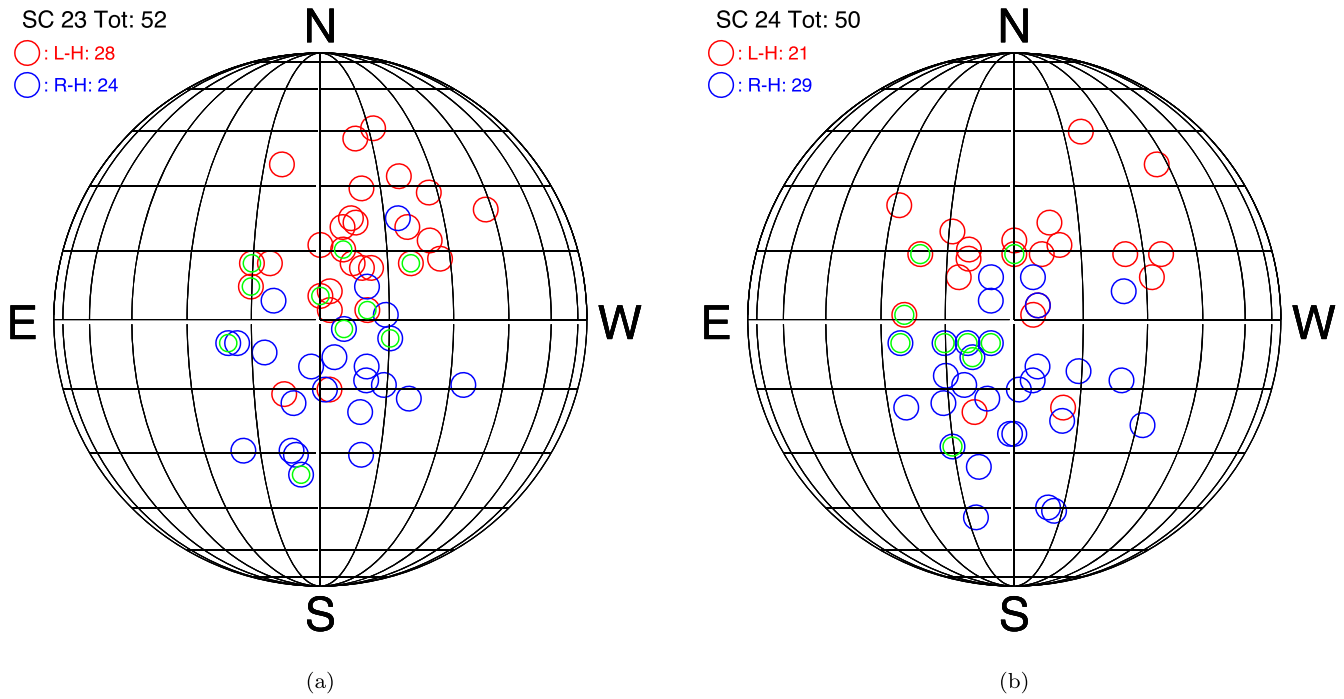

(a) (b)

Figure 1. Relation between CME solar source locations and the handedness of associated MCs at 1 au for (a) 52 MC-CMEs in SC 23 and (b) 50 MC-CMEs in SC 24. Blue and red circles represent the RH (positive) helicity and LH (negative) helicity MC events, respectively. The green circles superimposed on the blue or red circles represent stealth streamer-blowout CMEs, see details in Section 3.4).

Démoulin 1999; Green et al. 2007; Green & Kliem 2009). A sigmoid can have two forms: forward and reverse S-shape, indicating positive and negative helicity, respectively (Pevtsov et al. 1997; Green et al. 2007).

The solar source data we used in the study are from https://solarmonitor.org, which includes the SDO AIA and Helioseismic and Magnetic Imager (HMI; Scherrer et al. 2012), the SOHO Extreme ultraviolet Imaging Telescope (EIT; Delaboudinière et al. 1995), and the SOHO Michelson Doppler Imager (MDI; Scherrer et al. 1995). Soft X-ray data are from the X-Ray Telescope (XRT; Golub et al. 2007) on board Hinode and the Yohkoh Soft X-ray Telescope (SXT; Tsuneta et al. 1991). In addition, we use EUV images from the STEREO Extreme Ultraviolet Imager (EUVI; Wuelser et al. 2004) to study eruption signatures above the limb.

Our master event tables are located at https://cor1.gsfc.nasa.gov/catalog/MC-CME/MC_CME_master_sc23.html (SC 23) and https://cor1.gsfc.nasa.gov/catalog/MC-CME/MC_CME_master_sc24.html (SC 24), which list CME date, time, and EFR fitting parameters; solar source location, X-ray class, source type, and PIL tilt angle; MC type, helicity, and tilt angle, and links to MC fitting plots and parameters.

3. Results

3.1. Relation between CME Source Locations and MFR Helicity Signs

Figure 1 plots the relation between CME solar source locations and helicity signs of the associated MCs at 1 au for (a) 52 MC-CME pairs in SC 23 and (b) 50 such pairs in SC 24. The CME source locations are marked in the heliographic plot with blue and red circles representing the right-handed (RH, positive) and left-handed (LH, negative) helicity MC-CME events. From the plot, we can see that most MC-CME events follow the hemispheric-helicity rule, i.e., the northern (southern) magnetic fields tend to have a negative (positive) helicity, which has been observed by many statistical studies (Bothmer & Schwenn 1998; Wang 2013, and references therein). In the northern hemisphere, four (five) events in SC 23 (24) did not follow the hemispheric-helicity rule. In the southern hemisphere, only two out of 24 events in SC 23 and two out of 29 events in SC 24 did not follow the general helicity rule. There is a total of 13 (∼13%) exceptional events and the general helicity rule holds true in ∼87% of our 102 events.

3.2. Orientations of CME-FRs and MCs

In Figure 2, we plot the distribution of the tilt angles of (a) CME-FRs and (b) MCs, and (c) the distribution of rotation angles (MC tilt angles minus CME-FR tilt angles) for SC 23 and (d)–(f) for SC 24. The figure is in polar coordinates (r, α), where the radial values are the arbitrary event numbers used to separate the points in the plot; the tilt angle α is defined as the angle from east to the axial direction of the FR, with CW as positive. Similar to Figure 1, we group the events according to their helicity signs in order to look for a possible helicity-rotation pattern. In Figures 2(a) and (d), we find that the CME-FR tilt angles tend to be concentrated in the vicinity of 45°–225° and 135°–315° diagonals (marked by dashed lines in the figure), where 45° and 225° are in the northeast (NE) and southwest (SW) directions, and 135° and 315° in the northwest (NW) and southeast (SE) directions, respectively.

In the figure, we can see that RH (blue) events tend to lie in the NW–SE direction and LH (red) events in the NE–SW direction. We divide the selected events into three groups: (1) low inclination (L-inl; ±30° within the E–W direction), (2) mid inclination (M-inl; 30°–60° around diagonal), and (3) high inclination (H-inl; ±30° within the N–S direction). In SC 23, there are 16, 21, and 15 events in the L-, M-, and H-inl groups,

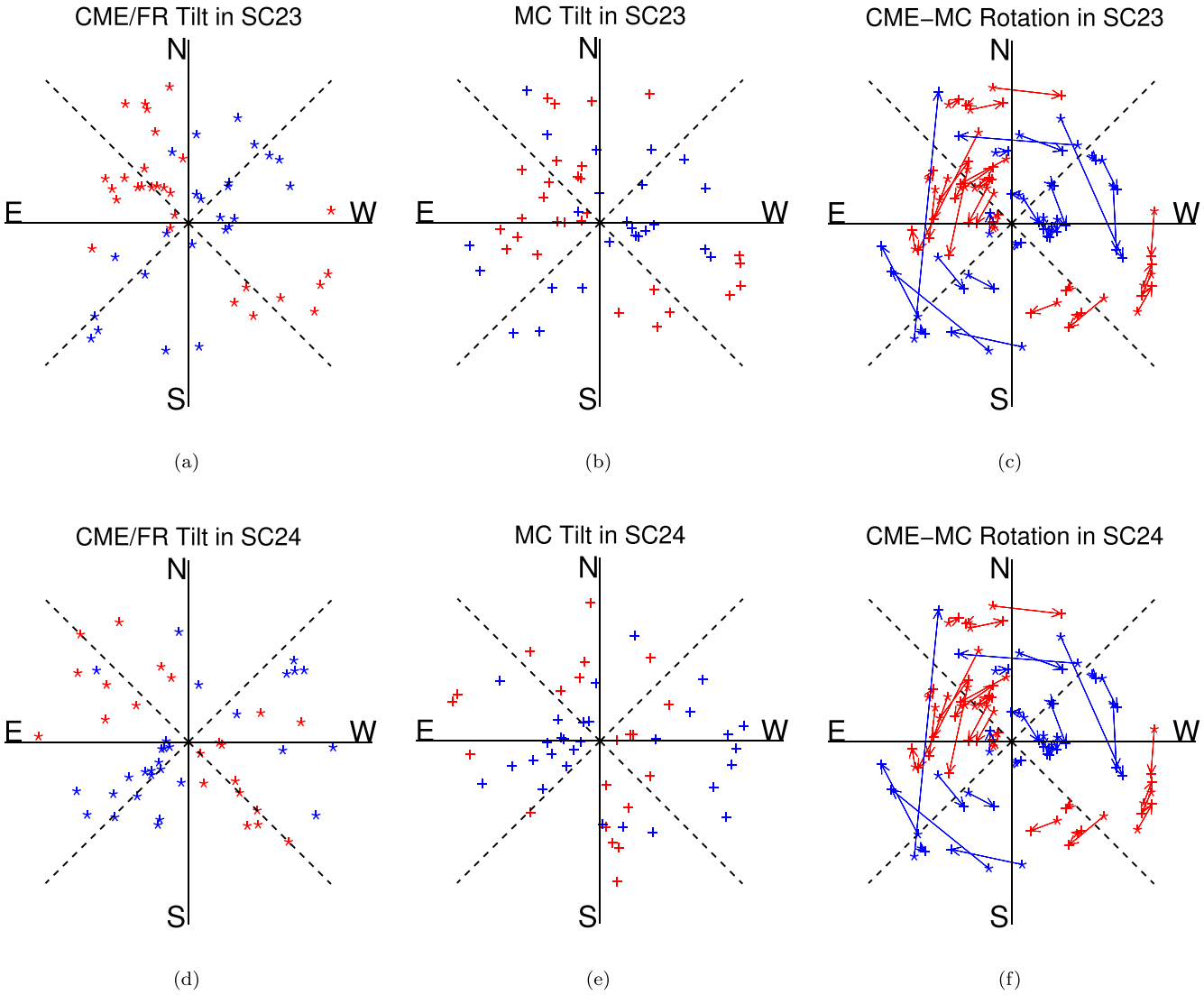

Figure 2. Distributions of (a) CME-FR tilt angels, (b) MC tilt angles, and (c) visual presentation of the rotations between MC-CME axial field directions for SC 23 and (d)–(f) for SC 24. In the plot, asterisks and plus symbols represent MC and CME-FR events, respectively.

respectively, where the diagonal events are of the plurality (∼40%). In SC 24, similarly, there are 15, 26, and nine in the three groups and the diagonal group (∼52%) is the predominate group.

Compared to CME-FRs, the MC events are more spread out and become less concentrated around the diagonal directions. There are 25, 12, and 15 (24, 11, and 15) events in the three groups in SC 23 (24). Due to the rotation (or combined rotation with deflection), the E–W type predominates the MC events with ∼50% in both SC 23 and SC 24. This result is consistent with Yurchyshyn's (2008) observations. On the one hand, the high-latitude events tend to be deflected by the global dipolar field, which guides the MFRs toward CNLs. On the other hand, the axial field rotations tend to have the MFRs aligned with the CNLs, which are mostly in low inclinations relative to the equator near the solar minima (see details in Section 3.4). In Figures 2(c) and (f), we present a visual representation of the rotation between MC-CME tilt angles.

Another interesting finding is that the PIL axial fields in the MFRs gradually change their directions from NE to SW (or NW to SW) following the solar pole reversal at the maximum. The change in the PIL axial field direction occur mostly in the filament CMEs, including both polar crown filaments and low-latitude filaments, and in stealth CMEs. As the solar cycle evolves, the filament CMEs during the declining phase and minima are located at lower latitudes than those in the rising phase, and the stealth CMEs tend to be closer to the equator. Similar patterns were also noted in previous works by Gopalswamy et al. (2008), Marubashi et al. (2015), and Palmerio et al. (2018). Our results are consistent with the early observations in Bothmer & Rust (1997), where they found that the predominant axial field directions of MCs reverse at the sunspot maximum. Lepping & Wu (2007) studied the variation of MCs during SC 23 and found that the change of MC types from south to north (S–N) to N–S (with E–W orientations) agrees with the global field change as predicted by Bothmer & Rust (1997). A possible cause is that the filament CMEs tend to be generated in such a PIL boundary (among dispersed adjacent PILs), where (1) the magnetic polarity change across the PIL matches the polarity change of the global dipolar field across sector boundaries and (2) the sheared field and rotation field of the PIL follows the hemispheric-helicity rule. The magnetic field configuration in these CME-producing PIL boundaries is similar to that in the Hale sector boundaries

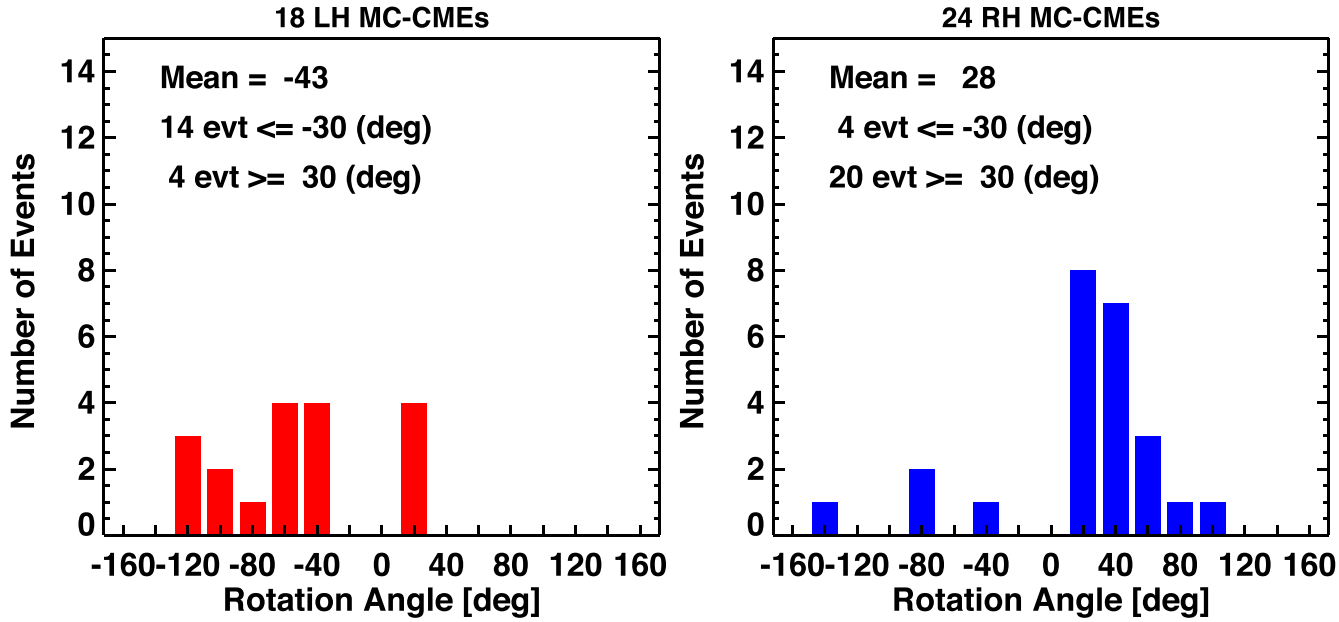

(a) (b)

Figure 3. Histogram of rotation angles between MC-CMEs, i.e., MC tilt angles minus CME-FR tilt angles, for (a) 18 LH events and (b) 24 RH events with rotations $>30°$.

(Svalgaard & Wilcox 1976), which are found to be the most probable locations for solar activities, such as flares and CME-capable ARs to occur (e.g., Svalgaard et al. 2011; Gyenge et al. 2017; Loumou et al. 2018).

3.3. Rotations of MC-CME Events

Figure 3 presents the histogram of MC-CME rotation angles for (a) 18 LH events and (b) 24 RH events with rotations $>30°$. It shows that for both LH and RH cases, most of the events follow the expected helicity-rotation relation, i.e., the RH and LH events tend to rotate CW and CCW, respectively. In Figure 3(a), 14 LH events (78% of 18) have a negative (CCW) rotation, and four LH events have a positive (CW) rotation. In Figure 3(b), 20 (4) RH events rotate CW (CCW). There is no obvious rotation pattern for the events with rotation angles $<30°$ (not shown in the plot).

It should be noted that taking into account an uncertainty of $\pm 20°$ in determining both the CME-FR and the MC tilt angle (e.g., Yurchyshyn 2008; Palmerio et al. 2018), one might expect a difference between MC-CME orientations up to $\pm 40°$ (in the worst scenario) even if there is no signification rotation. In this study, we consider events with rotations $>40°$ as rotational events. In our data set, we find $\sim$25% (25 out of 102) rotational events. For the other $\sim$75% of the 102 events, the MFR tilt angles near the Sun match in situ within $\pm 40°$.

Figure 4 shows two examples of the MC-CME events. The top panels show an example with no significant rotation and on 2012 June 14. The bottom panels show an example with a rotation $>100°$ on 2015 December 16. The panels from left to right are the SDO/AIA 131 Å EUV image, HMI magnetogram, and EFR fitting model (green wireframe) overlaid on the LASCO C2 image. The forward sigmoids before eruption marked by red curves in (a) and (d) suggest a positive helicity. The PIL orientations marked by red arrows in (b) and (e) are inferred from a TG/SG AR in (b) and an SG AR in (e). Red arrows in (c) and (f) denote the CME orientations obtained from the EFR model fitting. For the 2012 June 14 event, the tilt angles in the PIL, CME, and MC are $-31°$, $-15°$, and $-16°$, respectively. The change in the axial tilt in the PIL and the MC is $\sim 15°$, and the CME and the MC are almost aligned with each other. For the 2015 December 16 event, the tilt angles in the PIL, CME, and MC are $-24°$, $-140°$, and $-158°$. The rotations between the MC-PIL and the CME-PIL tilt angles are $-134°$ and $-116°$, respectively. Therefore, $\sim$87% of the rotation occurred in the extended corona and $\sim$13% occurred in the heliosphere.

Table 1 lists our comparison of the MFR axial tilts in PILs, CMEs, and MCs for the 25 events with rotations $>40°$. The results show that there is a clear pattern in these rotational events, i.e., LH (RH) events rotated CCW (CW). Most (92%) events except events R23-9 and R24-12 follow the expected helicity-rotation pattern. In Table 1, last column, we list the contribution of the CME rotation to the total rotation from the Sun to Earth. For $\sim$56% (14) events, more than 62% of the rotation occurred within the CMEs in the extended corona.

Of the 25 events, five events have rotations greater than $100°$ and 20 events have rotations ranging from 43°–86°, with a mean value of 61°. Among these 20 events, there are 12 events associated with filament eruptions and eight events associated with small to modest X-ray flares ($\leqslant$M2.2). All of the five large rotational events are flare CMEs, which are associated with a flare class ranging from B9.5–M8.7. In general, the MC-CME events occurring near solar minima experienced smaller rotations than the events occurred around more active phases. There is one exceptional event (R23-12), which occurred on 2007 May 19 and underwent a large rotation of 111°. It is a widely studied event that originated from a highly nonpotential AR with a complex magnetic field configuration (e.g., Li et al. 2008; Kilpua et al. 2009).

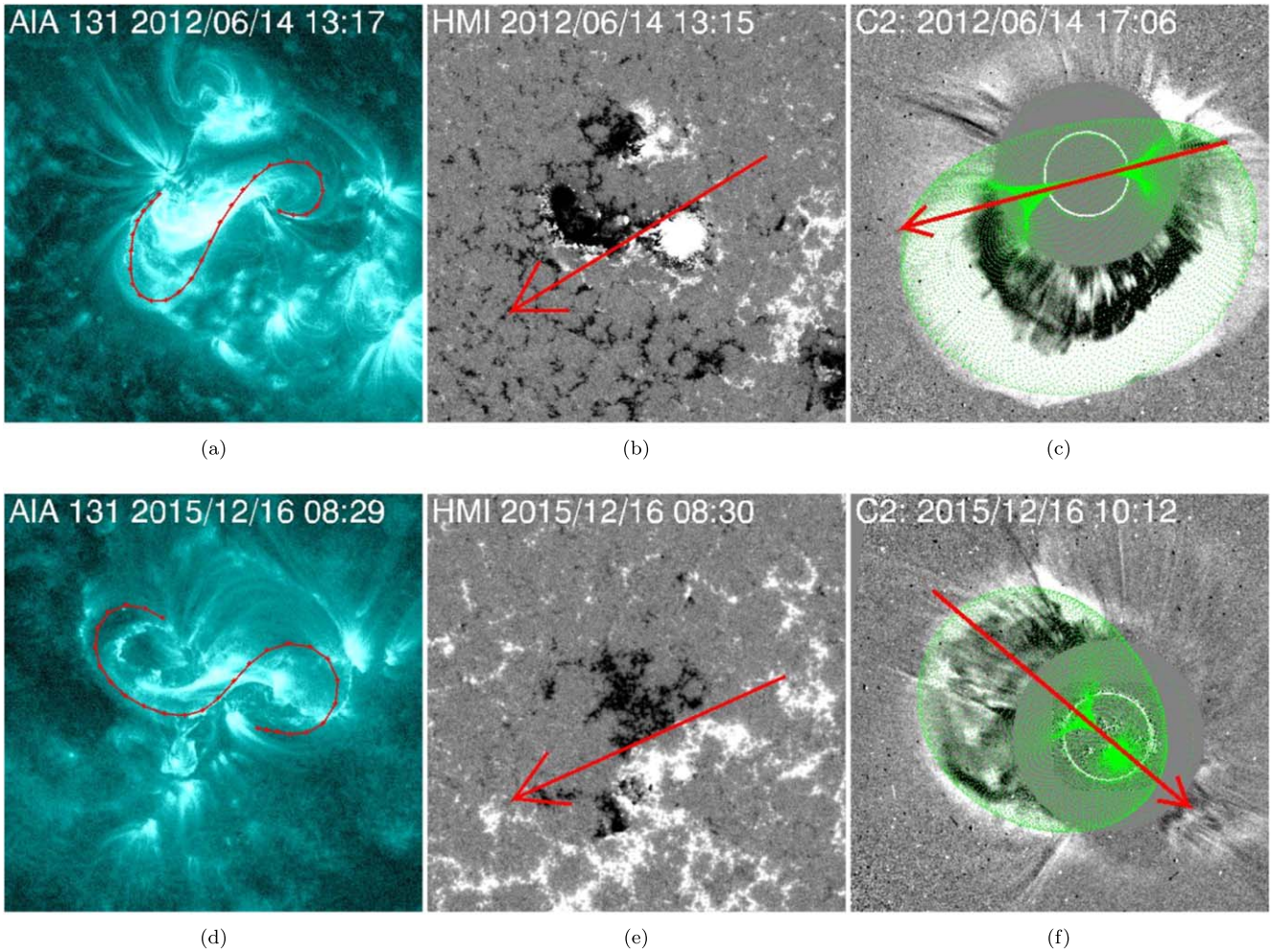

Figure 4. EUV and HMI observations of the solar sources for two events: (a)–(c) the SDO/AIA 131 (Å) EUV image, the HMI magnetogram, and the EFR fitting model (green wireframe) overlaid on the C2 image on 2012 June 14, showing an example of no rotation. (d)–(f) show an example on 2015 December 16, with a rotation greater than 100°. The red curves in (a) and (d) indicate forward sigmoids and red arrows in (b) and (e) mark the FR axial directions inferred from a TG/SG AR (b) and a SG AR (e). Red arrows in (c) and (f) denote the tilt angles of the CMEs.

The 2015 December 16 event shown in Figures 4(d)–(f) is one of the exceptional events that did not follow the helicity-rotation pattern. Liu et al. (2018) carried out a case study for this event using a nonpotential field model. They found that the CME was deflected largely in both latitude and longitude to the NE, due to a large gradient in the magnetic energy distribution. A similar negative rotation was obtained in their study. It is not clear that the event was rotated in the opposite sense, or the large CME deflection (with one of the footpoints disconnected) overruled the expected sense of rotation (e.g., Vourlidas et al. 2011; Nieves-Chinchilla et al. 2012).

3.4. Stealth Streamer-blowout CMEs and CNLs

To study the MC-CME events over the full solar cycles, our data set includes 19 stealth CMEs (10 in SC 23 and nine in SC 24) that occurred near the solar minima.

The stealth CMEs are typical of slow streamer-blowout CMEs with no apparent eruptive signatures (e.g., flares, EUV dimming and waves, and filament eruptions) observed in the solar disk (Robbrecht et al. 2009). The earthward stealth CMEs tend to be missed by LASCO but can be observed by STEREO SECCHI as FR-like CMEs. Also, in STEREO EUVI images, they often appear as Y-shaped concave features above the limb, which lift off from large heights and develop into the core of the CMEs (e.g., Xie et al. 2009).

Of nine stealth CMEs in SC 24, six were missed by LASCO and three appeared in LASCO as very faint CMEs. To confirm all these stealth CMEs are streamer-blowout CMEs, we apply the EFR model fit to STEREO A and B observations to obtain the CME locations, we then compare them with the CNL locations by overplotting them on the Wilcox Solar Observatory (WSO) source surface map, which shows the polarity distribution and the CNL location.

Figure 5 shows an example of the stealth CMEs on 2009 June 22 06:48 UT, where the CME location (marked by the red circle) is overplotted on the WSO source surface map at height of 2.5 *Rs*. We can see that the CME was almost located at the center of the CNL. By comparing the CME and the CNL locations, we find that all nine stealth CMEs in SC 24 are in the vicinity of the CNLs near the solar equator (within $\pm 30^{\circ}$).

For the 10 stealth CMEs in SC 23, we assume that they have the MFR axis aligned with the CNL. Due to lack of STEREO quasi-quadrature measurements, we use CNL locations as a proxy of the CME locations. First, we estimated the CME time using the average MC speed, then we find the associated CNL location in the WSO map. The tilt angle of the CNL is

Table 1
List of Events with Rotations >40° between MC-PIL Tilt Angles[a]

Event No.	CME			Solar Source				MC		Rotation	
	Date	Time (UT)	α_1 (°)	Loc	X-Ray	Type	α_0 (°)	H_{MC}	α_2 (°)	Total (°)	CME%
R23-1	1996/12/19	15:21	15	S13W10	C2.3	SG	−25	R	26	51	0.78
R23-2	1997/01/06	15:10	120	S18E06	A1.1	SG	117	R	178	61	0.05
R23-3	1997/05/12	05:30	58	N21W08	C1.3	SG	59	L	0	−59	0.02
R23-4	1997/07/30	04:45	10	N42W10	⋯	EP	55	L	1	−54	0.83
R23-5	1997/10/06	15:28	150	S30E06	⋯	EP	137	R	182	45	0.29
R23-6	1998/06/21	04:39	45	N17W25	C2.7	TG	85	L	38	−47	0.85
R23-7	1999/04/13	03:30	−10	N16E00	B4.3	EP	51	L	−27	−78	0.78
R23-8	2001/05/25	04:06	70	N32W20	⋯	EP	70	L	−16	−86	0.00
R23-9	2002/03/15	23:06	130	S08W03	M2.2	TG	130	R	59	−71	0.00
R23-10	2003/08/14	20:06	115	S10E02	C3.8	SG	115	R	197	82	0.00
R23-11	2004/07/22	08:30	−10	N04E10	C5.3	TG	−80	R	−22	58	1.21
R23-12	2007/05/19	13:24	70	N07W10	B9.5	TG	−50	R	61	111	1.08
R24-1	2008/12/12	08:54	225	N44W20	⋯	EP	225	L	178	−47	0.00
R24-2	2009/03/10	02:54	2	S28E15	⋯	PEP*	2	R	61	59	0.00
R24-3	2009/06/22	06:48	25	S08E09	⋯	PEP*	−15	R	48	63	0.63
R24-4	2009/12/26	08:45[b]	−10	S47E12	⋯	EP	−45	R	5	50	0.30
R24-5	2010/04/03	10:33	−70	S25E00	B7.4	SG	−80	R	−37	43	0.23
R24-6	2010/06/16	14:54	20	S25E01	⋯	EP	−38	R	30	65	0.89
R24-7	2012/10/08	21:10	5	S19W11	BRT	TG	15	L	−94	−109	0.09
R24-8	2013/04/11	07:24	120	N09E12	M6.5	SG	225	L	121	−104	1.01
R24-9	2013/06/02	16:25[b]	−15	N14W25	⋯	EP	35	L	−46	−81	0.62
R24-10	2013/06/30	03:12	−96	S11W14	⋯	EP	−46	R	−120	−74	0.68
R24-11	2014/12/17	05:00	50	S20E09	M8.7	TG	170	L	52	−118	1.02
R24-12	2015/12/16	09:36	−140	S13W04	C6.6	SG	−24	R	−158	−134	0.87
R24-13	2017/05/23	05:00	175	N03W05	⋯	EP	142	R	190	48	0.69

Notes.
[a] Columns 1–4: event No., CME data, time, and EFR-fit tilt angle. Columns 5–9: solar source location, X-ray class, source type, and PIL tilt angle (EP = eruptive prominence or filament disappearance, SG = sigmoid flare, TG = tongue-shaped flare). Columns 10–12: MC type, helicity, and tilt angle. Columns 13–14: total rotation (MC-PIL) and percentage of CME rotation/total rotation.
[b] STEREO-only event: CME time is the first appearance time in COR1.

measured in the CW direction from the east. Like the CME tilts, they also have a 180° ambiguity. We apply the general helicity rule to determine their helicity signs and axial directions.

By comparing the MC and CNL orientations, we find that most of the MCs (∼89%, 17 out of 19) rotated by less than 20° from the CNL orientations. For the two (∼11%) exceptional events (SC 24-03 and SC 24-04), the MCs rotated about ∼60° from the CNLs. Also, the MFR helicity signs inferred from the CNL locations match those in MCs. The above results suggest that for most of the stealth CMEs, we can use CNL locations and tilt angles combined with the hemispheric-helicity rule to predict the magnetic structures in MCs.

Finally, we extend the comparison to all the events during the rising phase of the cycles, and we find that 72% of the events in our data set have the MC orientations aligned with the CNL orientations, and ∼28% of the events show the difference between the MC and CNL orientations up to ∼35°–79°.

4. Summary and Discussion

This work aims to contribute to a better understanding of the relationships between MCs, CME-FRs, and the MFRs at the Sun and to improve the prediction of the magnetic structures at 1 au. Our main conclusions are summarized below.

(1) We conducted a comprehensive statistical analysis using a data set spanning two full cycles. To study as many events as possible, we examined the 19 stealth CMEs near the solar minimum, including nine events in SC 24 and 10 events in SC 23. Our results show that for 89% of the stealth CMEs, we can use the CNL locations and tilt angles to correctly predict the MC magnetic structures. For two exceptional events (SC 24-02 and 03), the difference between the MC and CNL orientations can reach up to ∼60°.

(2) We confirmed that the hemispheric-helicity rule holds true for 87% of the events in our data set, i.e., the MFRs in the northern (southern) hemisphere tend to have left-handed (right-handed) helicity. For the 13 exceptional events, the MFR helicity signs estimated from the solar source proxies, e.g., the coronal arcade skew, sigmoid, and magnetic tongue method, agreed with the helicity signs in the MCs.

(3) Statistically, for ∼46% of the MC-CME pairs we examined, the MFR tilt angles near the Sun were concentrated in the vicinity of the 45°–225° (NE–SW) and 135°–315° (NW–SE) diagonals. The MC tilt angles had ∼48% lying within ±30° from the E–W direction, due to rotations combined with deflections from high and mid inclinations toward low inclinations. This result is consistent with the observations that the MC orientations tend to align with the CNLs, which mostly are in the low inclination relative to the equator near the solar minima.

(4) Over the two full solar cycles, the MFR axial fields in the filament CMEs show a trend of flipping around each solar pole

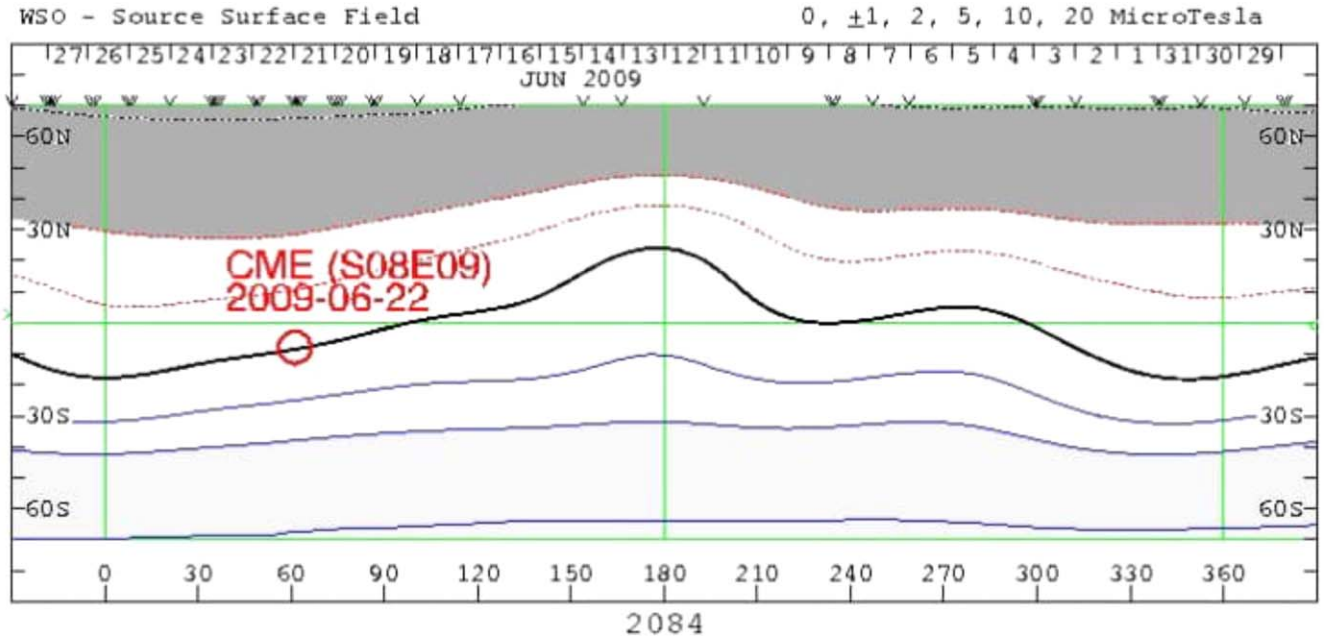

Figure 5. WSO source surface synoptic map calculated for the height of 2.5 *Rs*. Dark gray contours represent negative fields, light gray contours, positive fields. Thick solid line is the CNL. The source location of the 2009 June 22 CME, marked by the red circle, is overplotted on the map showing the relative location between the CME source and the CNL.

reversal. As the solar cycle progresses, the CME-FR sources gradually move toward the solar equator, in a similar pattern as shown in the butterfly diagram. The CME-FRs tend to be generated along the PIL boundaries, where the MFR chirality obeys the hemispheric-helicity rule and the poloidal field change agrees with the global solar field change, a configuration similar to that in the Hale sector boundary.

(5) Around 25% (25 of 102) events have rotations greater than 40° between MC-PIL tilts. For ∼56% of cases, the rotations occurred within the COR2 field of view, where the MC axial directions can be predicted from the CME-FR tilt angles obtained from the EFR fitting.

(6) Most (92%) of the rotational events followed the helicity-rotation pattern, i.e., RH (LH) events rotate CW (CCW).

(7) During the solar minima, ∼72% of the MCs have their axial orientations aligned along the CNL directions, and for ∼28% cases, the difference between the MC and CNL orientations is greater than 35°.

Bothmer & Schwenn (1998) proposed a prediction scheme, known as the Bothmer–Schwenn scheme, to relate the helicity and the MFR axial direction within a CME to the global field change, polarity of sunspot pairs, the solar cycle number, and the CME hemisphere. The reliability of the hemispheric rule, however, remains controversial due to the past observational instrument limits. Also, a wide distribution of the MC tilt angles and rotations make the prediction scheme less effective. Using Fe XII stalks observed in EUV images, Wang et al. (2013) confirmed that greater than ∼80% of quiescent filaments and filament channels that form during the decay of ARs follow the general helicity rule. Wang (2013) further argued that the overall consensus of ∼60%–70% of ARs following the hemispheric-helicity rule may be underestimated; the actual percentage was likely to be similar to the >80% found for quiescent filaments. They pointed out that the reason for the underestimate is that the axial field component in new ARs is masked by the much stronger transverse field and is difficult to measure reliably; as the transverse field is gradually canceled at the PIL, the axial field begins to dominate (as in quiescent filaments) and its direction becomes much clearer. The present study provides support for this argument. Our analysis results show that the hemispheric-helicity rule holds true for almost all quiet Sun filament events and for ∼72%–83% of the AR events. For events not obeying the rule, we found that the magnetic helicity signs determined by either the magnetic tongue or sigmoid method were opposite to the general helicity but matched the helicity signs in the associated MCs. The results above provide a possible way to reliably predict the FR helicity and its initial axial direction. By combining our work with the work of Gopalswamy et al. (2017) to estimate the axial field intensity using the reconnected flux, we could better estimate the initial magnetic FR structure.

The difficult part is how to predict the magnetic FR orientation for the rotational events. Based on our results, (5)–(7), there is the possibility to utilize the CME tilt angles and CNL tilt angles to improve the prediction. However, both methods have a larger than expected number of exceptional cases. Yurchyshyn et al. (2007) and Yurchyshyn (2008) found similar results. They suggested that the events showed no agreement between the CMEs, and MCs tend to have MCs aligned with CNLs, and speculate that the heliospheric current sheet (HCS) had a big influence on such cases. On the other hand, Isavnin et al. (2014) used a 3D MHD model to study the evolution of 14 CMEs occurred during the solar minimum near SC 23 and SC 24. They found that the FRs tend to stay near the HCS but they are not necessarily aligned with it. They suggested that some non-alignment events seem to be influenced by the relative location of fast- and slow-wind streams. Similarly, in our study, there are ∼28% of the events that show a difference between MC and CNL orientations of >35°. Right now, it is not clear what the controlling conditions are for the non-alignment events. We agree that other factors, such as structured solar wind streams, CIRs, and interactions

between CMEs and fast wind streams may play important roles. Further investigations are needed.

The authors would like to thank the support of STEREO, SOHO, SDO, WIND, WSO, Yohkoh, and Hinode teams. We acknowledge the STEREO COR1, LASCO CDAW, GMU SEEDS COR2 catalogs, online OMNI data, and solarmonitor.org for making solar source data available online. The SECCHI data are produced by an international consortium of the NRL, LMSAL, NASA GSFC (USA), RAL and the University of Birmingham (UK), MPS (Germany), CSL (Belgium), and IOTA and IAS (France). SOHO is a project of international cooperation between ESA and NASA.

ORCID iDs

H. Xie https://orcid.org/0000-0002-0058-1162
N. Gopalswamy https://orcid.org/0000-0001-5894-9954
S. Akiyama https://orcid.org/0000-0002-7281-1166

References

Bothmer, V., & Rust, D. 1997, in Coronal Mass Ejections (Geophys. Monogr. Ser. 99) ed. N. Crooker, J. A. Joselyn, & J. Feynman (Washington, DC: American Geophysical Union), 139
Bothmer, V., & Schwenn, R. 1998, AnGeo, 16, 1
Brueckner, G. E., Howard, R. A., Koomen, M. J., et al. 1995, SoPh, 162, 357
Burlaga, L. F. 1988, JGR, 93, 7217
Burlaga, L., Sittler, E., Mariani, F., & Schwenn, R. 1981, JGR, 86, 6673
Canfield, R. C., Hudson, H. S., & McKenzie, D. E. 1999, GeoRL, 26, 627
Chen, J., Howard, R. A., Brueckner, G. E., et al. 1997, ApJL, 490, L191
Chen, P. F. 2011, LRSP, 8, 1
Cheng, X., Zhang, J., Ding, M. D., Liu, Y., & Poomvises, W. 2013, ApJ, 763, 43
Cheng, X., Zhang, J., Liu, Y., & Ding, M. D. 2011, ApJL, 732, L25
Delaboudinière, J. P., Artzner, G. E., Brunaud, J., et al. 1995, SoPh, 162, 291
Dere, K. P., Brueckner, G. E., Howard, R. A., Michels, D. J., & Delaboudiniere, J. P. 1999, ApJ, 516, 465
Domingo, V., Fleck, B., & Poland, A. I. 1995, SoPh, 162, 1
Fan, Y., & Gibson, S. E. 2004, ApJ, 609, 1123
Gibson, S. E., & Low, B. C. 2000, JGRA, 105, 18187
Golub, L., Deluca, E., Austin, G., et al. 2007, SoPh, 243, 63
Gopalswamy, N. 2006, SSRv, 124, 145
Gopalswamy, N., Akiyama, S., Yashiro, S., Michalek, G., & Lepping, R. P. 2008, JASTP, 70, 245
Gopalswamy, N., Akiyama, S., Yashiro, S., & Xie, H. 2018, in IAU Symp. 335, Space Weather of the Heliosphere: Processes and Forecasts, ed. C. Foullon & O. E. Malandraki (Cambridge: Cambridge Univ. Press), 258
Gopalswamy, N., Lara, A., Lepping, R. P., et al. 2000, GeoRL, 27, 145
Gopalswamy, N., Mäkelä, P., Akiyama, S., et al. 2013a, SoPh, 284, 17
Gopalswamy, N., Mäkelä, P., Xie, H., Akiyama, S., & Yashiro, S. 2009, JGRA, 114, A00A22
Gopalswamy, N., Nieves-Chinchilla, T., Hidalgo, M., et al. 2013b, SoPh, 284, 1
Gopalswamy, N., Shimojo, M., Lu, W., et al. 2003, ApJ, 586, 562
Gopalswamy, N., Xie, H., Akiyama, S., Mäkelä, P. A., & Yashiro, S. 2014, EP&S, 66, 104
Gopalswamy, N., Yashiro, S., Xie, H., Akiyama, S., & Mäkelä, P. 2015, JGRA, 120, 9221
Gopalswamy, N., Yashiro, S., Akiyama, S., & Xie, H. 2017, SoPh, 292, 65
Green, L. M., & Kliem, B. 2009, ApJL, 700, L83
Green, L. M., Kliem, B., Török, T., van Driel-Gesztelyi, L., & Attrill, G. D. R. 2007, SoPh, 246, 365
Gyenge, N., Singh, T., Kiss, T. S., Srivastava, A. K., & Erdélyi, R. 2017, ApJ, 838, 18
Howard, R. A., Moses, J. D., Vourlidas, A., et al. 2008, SSRv, 136, 67
Illing, R. M. E., & Hundhausen, A. J. 1985, JGR, 90, 275
Isavnin, A., Vourlidas, A., & Kilpua, E. K. J. 2014, SoPh, 289, 2141
Kaiser, M. L., Kucera, T. A., Davila, J. M., et al. 2008, SSRv, 136, 5
Kay, C., Gopalswamy, N., Xie, H., & Yashiro, S. 2017, SoPh, 292, 78
Kilpua, E. K. J., Liewer, P. C., Farrugia, C., et al. 2009, SoPh, 254, 325
Krall, J., & St. Cyr, O. C. 2006, ApJ, 652, 1740
Lemen, J. R., Title, A. M., Akin, D. J., et al. 2012, SoPh, 275, 17
Lepping, R. P., Berdichevsky, D. B., Wu, C. C., et al. 2006, AnGeo, 24, 215
Lepping, R. P., Jones, J. A., & Burlaga, L. F. 1990, JGR, 95, 11957
Lepping, R. P., & Wu, C. C. 2007, JGRA, 112, A10103
Lepping, R. P., Wu, C. C., Berdichevsky, D. B., & Szabo, A. 2011, SoPh, 274, 345
Lepping, R. P., Wu, C. C., Berdichevsky, D. B., & Szabo, A. 2015, SoPh, 290, 2265
Lepping, R. P., Wu, C. C., Berdichevsky, D. B., & Szabo, A. 2018, SoPh, 293, 65
Lepping, R. P., Wu, C. C., Berdichevsky, D. B., & Szabo, A. 2020, SoPh, 295, 83
Li, Y., Lynch, B. J., Stenborg, G., et al. 2008, ApJL, 681, L37
Liu, Y. A., Liu, Y. D., Hu, H., Wang, R., & Zhao, X. 2018, ApJ, 854, 126
Lopez, R. E., & Freeman, J. W. 1986, JGR, 91, 1701
Loumou, K., Hannah, I. G., & Hudson, H. S. 2018, A&A, 618, A9
Luoni, M. L., Démoulin, P., Mandrini, C. H., & van Driel-Gesztelyi, L. 2011, SoPh, 270, 45
Lynch, B. J., Antiochos, S. K., Li, Y., Luhmann, J. G., & DeVore, C. R. 2009, ApJ, 697, 1918
Mäkelä, P., Gopalswamy, N., Xie, H., et al. 2013, SoPh, 284, 59
Martin, S. F. 1998, in ASP Conf. Ser. 150, New Perspectives on Solar Prominences, ed. D. F. Webb, B. Schmieder, & D. M. Rust (San Francisco, CA: ASP), 419
Martin, S. F., Lin, Y., & Engvold, O. 2008, SoPh, 250, 31
McAllister, A. H., Hundhausen, A. J., Mackay, D., & Priest, E. 1998, in ASP Conf. Ser. 150, New Perspectives on Solar Prominences, ed. D. F. Webb, B. Schmieder, & D. M. Rust (San Francisco, CA: ASP), 430
Marubashi, K., Akiyama, S., Yashiro, S., et al. 2015, SoPh, 290, 1371
Möstl, C., Rollett, T., Frahm, R. A., et al. 2015, NatCo, 6, 7135
Nieves-Chinchilla, T., Colaninno, R., Vourlidas, A., et al. 2012, JGRA, 117, A06106
Nindos, A., Patsourakos, S., Vourlidas, A., Cheng, X., & Zhang, J. 2020, A&A, 642, A109
Palmerio, E., Kilpua, E. K. J., James, A. W., et al. 2017, SoPh, 292, 39
Palmerio, E., Kilpua, E. K. J., Möstl, C., et al. 2018, SpWea, 16, 442
Pesnell, W. D., Thompson, B. J., & Chamberlin, P. C. 2012, SoPh, 275, 3
Pevtsov, A. A., Canfield, R. C., & McClymont, A. N. 1997, ApJ, 481, 973
Robbrecht, E., Patsourakos, S., & Vourlidas, A. 2009, ApJ, 701, 283
Sarkar, R., Gopalswamy, N., & Srivastava, N. 2020, ApJ, 888, 121
Scherrer, P. H., Bogart, R. S., Bush, R. I., et al. 1995, SoPh, 162, 129
Scherrer, P. H., Schou, J., Bush, R. I., et al. 2012, SoPh, 275, 207
Sheeley, N. R. J., Martin, S. F., Panasenco, O., & Warren, H. P. 2013, ApJ, 772, 88
Shen, C., Wang, Y., Gui, B., Ye, P., & Wang, S. 2011, SoPh, 269, 389
Sterling, A. C., Moore, R. L., & Harra, L. K. 2011, ApJ, 743, 63
Svalgaard, L., Hannah, I. G., & Hudson, H. S. 2011, ApJ, 733, 49
Svalgaard, L., & Wilcox, J. M. 1976, SoPh, 49, 177
Titov, V. S., & Démoulin, P. 1999, A&A, 351, 707
Török, T., Kliem, B., & Titov, V. S. 2004, A&A, 413, L27
Tsuneta, S., Acton, L., Bruner, M., et al. 1991, SoPh, 136, 37
Veronig, A. M., Podladchikova, T., Dissauer, K., et al. 2018, ApJ, 868, 107
Vourlidas, A. 2014, PPCF, 56, 064001
Vourlidas, A., Colaninno, R., Nieves-Chinchilla, T., & Stenborg, G. 2011, ApJL, 733, L23
Wang, Y. M. 2013, ApJL, 775, L46
Wang, Y. M., & Berger, M. A. 2018, ApJ, 868, 66
Wang, Y. M., Sheeley, N. R. J., & Stenborg, G. 2013, ApJ, 770, 72
Wu, C. C., Lepping, R. P., & Gopalswamy, N. 2006, SoPh, 239, 449
Wuelser, J.-P., Lemen, J. R., Tarbell, T. D., et al. 2004, Proc. SPIE, 5171, 111
Xie, H., Gopalswamy, N., & St. Cyr, O. C. 2013, SoPh, 284, 47
Xie, H., Ofman, L., & Lawrence, G. 2004, JGRA, 109, A03109
Xie, H., St. Cyr, O. C., Gopalswamy, N., et al. 2009, SoPh, 259, 143
Yashiro, S., Gopalswamy, N., Mäkelä, P., & Akiyama, S. 2013, SoPh, 284, 5
Yurchyshyn, V. 2008, ApJL, 675, L49
Yurchyshyn, V., Hu, Q., Lepping, R. P., Lynch, B. J., & Krall, J. 2007, AdSpR, 40, 1821
Zhang, J., Cheng, X., & Ding, M.-D. 2012, NatCo, 3, 747